

Research Article www.acsami.org

Physics-Guided Neural-Network-Based Inverse Design of a Photonic—Plasmonic Nanodevice for Superfocusing

Boqun Liang, Da Xu, Ning Yu, Yaodong Xu, Xuezhi Ma, Qiushi Liu, M. Salman Asif, Ruoxue Yan, and Ming Liu*



Cite This: ACS Appl. Mater. Interfaces 2022, 14, 27397–27404



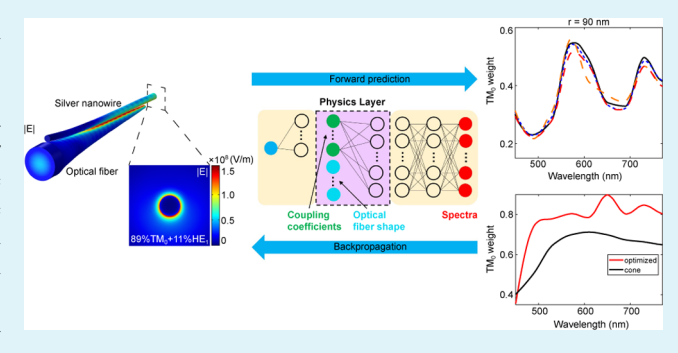
ACCESS I

III Metrics & More

Article Recommendations

Supporting Information

ABSTRACT: Controlling the nanoscale light-matter interaction using superfocusing hybrid photonic-plasmonic devices has attracted significant research interest in tackling existing challenges, including converting efficiencies, working bandwidths, and manufacturing complexities. With the growth in demand for efficient photonic-plasmonic input-output interfaces to improve plasmonic device performances, sophisticated designs with multiple optimization parameters are required, which comes with an unaffordable computation cost. Machine learning methods can significantly reduce the cost of computations compared to numerical simulations, but the input-output dimension mismatch remains a challenging problem. Here, we introduce a physics-



guided two-stage machine learning network that uses the improved coupled-mode theory for optical waveguides to guide the learning module and improve the accuracy of predictive engines to 98.5%. A near-unity coupling efficiency with symmetry-breaking selectivity is predicted by the inverse design. By fabricating photonic-plasmonic couplers using the predicted profiles, we demonstrate that the excitation efficiency of 83% on the radially polarized surface plasmon mode can be achieved, which paves the way for super-resolution optical imaging.

KEYWORDS: deep learning, neural network, superfocusing, plasmonic, on-demand design, silver nanowire

■ INTRODUCTION

Plasmonic structures can manipulate electromagnetic fields at the nanoscale and have inspired numerous applications, including chemical analysis microscopy, 1-3 signal processing, 4-6 and energy harvesting. 7-9 Converting light from a diffraction-limited photonic system to a subdiffraction-limited plasmonic system and transferring electromagnetic energy between different plasmonic structures to control light with unprecedented capability is crucial for high-efficiency energyharvesting applications, sensitive detectors, and super-resolution optical imaging. However, the significant mismatch in optical momentum k between different optical components, such as a photonic mode $(k \sim 10^6-10^7 \text{ m}^{-1})$ and a superfocused plasmonic hot-spot ($k \sim 10^9 \text{ m}^{-1}$), reduces the coupling efficiency between the two systems, forming an insurmountable gap that obstructs the development of highconversion-efficiency plasmonic applications. To tackle this problem, various types of superfocusing plasmonic structures have been invented to bridge the momentum mismatch that has orders of magnitude in difference. Among these structures, the adiabatic superfocusing on a conical metallic waveguide is particularly interesting due to its straightforward fabrication requirements and the potential for high spatial resolution imaging and has been broadly used in applications such as tipenhanced Raman scattering spectroscopy. 10 However, the superfocusing of a conical metallic waveguide is only applicable to the radially polarized fundamental transverse-magnetic (TM₀) surface plasmon polariton (SPP) mode, which is difficult to excite by a photonic or free-space beam with highconversion efficiency due to the mismatch in mode profiles and symmetry. The uncertainty of the weight of compressible TM₀ mode in the SPP launched on a metallic waveguide casts a shadow over superfocusing.¹¹ Recently, devices that combine the excitation ability of photonic structures and confining ability of plasmonic structures have attracted much attention. For instance, a photonic-plasmonic coupler based on Landau-Zener tunneling has been demonstrated for highexternal-efficiency superfocusing. 15 The energy-transfer efficiency in a Landau-Zener process is determined by the coupling coefficients between the two participating modes and the changing rate of the propagation constant along the

Received: March 22, 2022 Accepted: May 13, 2022 Published: June 1, 2022





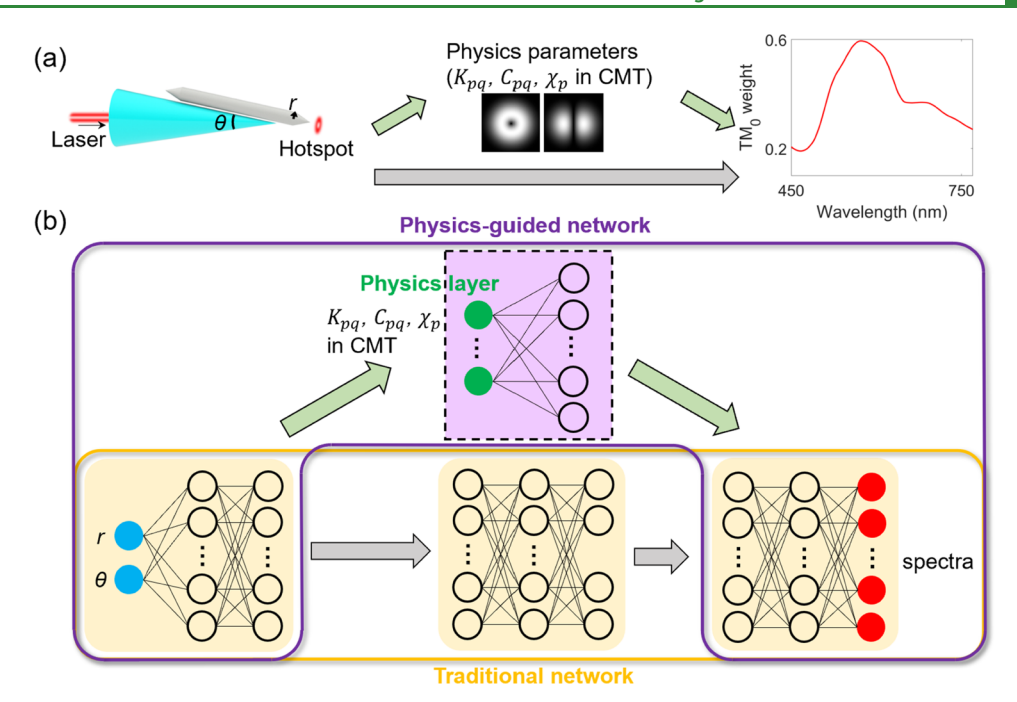


Figure 1. Schematics of the photonic–plasmonic coupler and the neural-network structure. (a) Coupler, consisting a tapered optical fiber and a silver nanowire, corresponds to a set of physics parameters based on the coupled-mode theory that determines the TM_0 -mode weight spectrum. (b) Structures of the traditional network (yellow box) and the physics-guided network (purple box).

propagation direction at the tunneling region. Since a plasmonic conical nanowire supports multiple SPP modes, but only the fundamental TM_0 SPP mode is desired, careful device designs are required to excite this TM_0 SPP mode and diminish the rest selectively. Due to the dimension of the coupler ($\sim 20~\mu m$ in length), such optimizations are impractical for conventional methods based on time-consuming simulations.

The inverse design of plasmonic structures for different applications is a challenging problem. Although data-driven methods based on neural networks (NNs) have achieved inverse design in different subjects, 17-28 the input-output dimension mismatch²⁹ and inverse network degeneracy problem³⁰ pose major challenges. In plasmonic-related machine learning designs, the design space usually has only a few parameters for a plasmonic element geometry, which is much less than the output responses, containing hundreds of data points for the optical properties at each wavelength. This mismatch has restrained the convergence of a neural network and inspired various methods, including introducing binarized input design parameters, 17 inserting down- and up-sampling layers, ²⁹ normalizing geometrical parameters with wavelengths, ³¹ or adding random noise ^{32,33} to compensate for the dimension mismatch. However, binary parameters sacrifice spectral details and cannot satisfy complex demands. The down- and up-sampling are equivalent to discarding functional data points and performing interpolation, respectively, which inevitably sacrifice some spectral details.³¹ Parameter normalization to operation wavelengths breaks down the output vectors to single data points, demanding extra steps for inverse design³¹ that increase random noise and make the model hard to decipher. 19 Recently, researchers interpreted the performance of NNs by using latent variables as a probabilistic representation of the design^{19,34} or explainable artificial intelligence approach.³⁵ However, they still require an extra variational autoencoder or calculations of feature contributions. As a consequence, a deep learning network design, which can compensate for the input—output mismatch and can be interpreted by physics theories, is in great demand. Researchers have tried various methods to overcome this degeneracy problem in inverse design, including using a tandem network or probability distributions to model design parameters, which make the NN more intricate and time consuming. Other methods such as genetic algorithms, automatic differentiations, have also been utilized to accelerate the optimization approach, but usually, an extra algorithm structure is required in these methods. Therefore, a simple inverse design method that can solve the degeneracy problem has drawn much interest.

In this paper, we design a physics-guided two-stage NN that employs the mode-coupling coefficients acquired through the coupled-mode theory as an intermediate training target to integrate the simplicity of mathematics, intuitiveness of the physics theory, and the power of the data-driven machine learning method. The proposed method also bridges the input-output dimension mismatch and predicts electromagnetic responses of the plasmonic structures as accurately as numerical simulations. In this NN, the design-performance relation can be directly interpreted by relying on a physics model describing underlying principles. Since the physicsguided method needs fewer layers than the traditional direct learning method for reasonable accuracy, this method can further simplify the NN structure and reduce the computation complexity. For the inverse design, we use a simple and general approach based on backpropagation with an analytical gradient. 44 An extra layer with design parameters as weights is attached to the fixed and trained forward prediction NN, accomplishing the on-demand design with minimal changes in the forward NN. Moreover, the backpropagation method can avoid the degeneracy problem because the forward network instead of the inverse network³⁰ is trained. Our work indicates

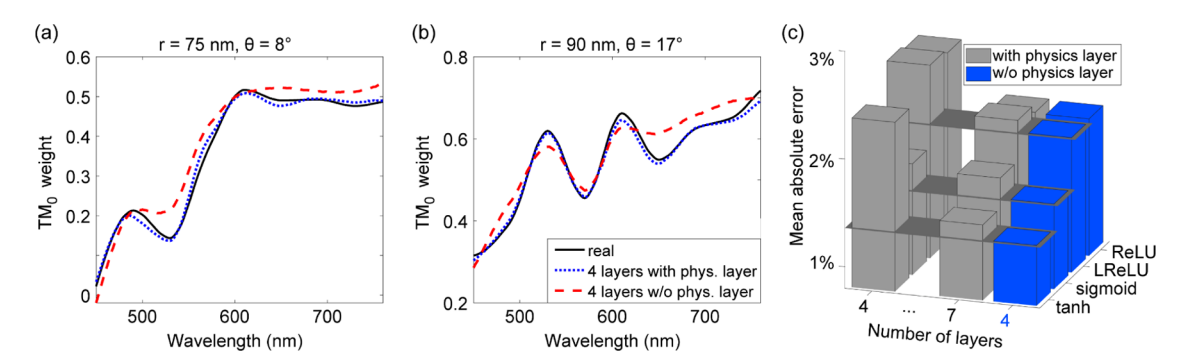


Figure 2. Evaluation of the deep-learning methods with and without the physics layer. (a) and (b) Example results with two sets of parameters: r = 75 nm, $\theta = 8^{\circ}$ and r = 90 nm, and $\theta = 17^{\circ}$. The blue dotted lines are from the physics-guided method and the red dashed lines represent the results of the traditional method without the physics layer. (c) MAE of different training methods, with different layer numbers and different activation functions used. Blue and gray bars correspond to the physics-guided method and the traditional methods without the physics layer.

that the design of complicated photonic—plasmonic structures can be realized by implementing compact network structures, which simplifies photonic and plasmonic design problems and accelerates related nanophotonics studies.

RESULTS AND DISCUSSION

The hybrid photonic—plasmonic structure consists of a linearly tapered optical fiber (OF) and a silver nanowire (AgNW), ¹⁵ as shown in Figure 1a. The NN takes two critical design parameters, namely, the fiber taper angle θ and AgNW radius r, as the input. The intensity of the fundamental transverse-magnetic (TM₀) SPP mode at the AgNW tip over the wavelength range of interest (450–770 nm with 2 nm interval) serves as the desired output (details in the Supporting information). This model has a tremendous mismatch between the two-dimensional input and the 161-dimensional output.

To verify the role of the physics-guided layer in the model, we first build, train, and test traditional NNs in a conventional manner. The input parameters are normalized to a similar magnitude to accelerate the training. Each fully connected layer is followed by an activation function to introduce nonlinearity. The performance of the networks is evaluated by the mean absolute error (MAE), defined as $\sum_i l_{pi} - t_i l$, where pi is the predicted TM_0 intensity and t_i is the ground truth of the TM_0 intensity. We also compared the performance of different activation functions, including the hyperbolic tangent (tan h), the sigmoid, the rectified linear unit (ReLU), and the leaky rectified linear unit (LReLU). As shown in Figure 2c, the MAE of NNs with the tanh activation function gives the best performance among activation functions with the same number of layers.

To incorporate the physics theory in machine learning, we construct a two-stage NN as an analog to the physics-based calculations, as shown in Figure 1b. The coupled-mode theory utilizes overlapping integrals of the electromagnetic fields to acquire different mode-coupling coefficients between the AgNW and OF with different diameters, which are used to evaluate the intensity evolution of each mode along the propagation direction. The two-stage NN first maps the two design parameters to 11 coupling coefficients between the two lowest-order SPP modes in AgNW (TM $_0$ and HE $_1$) and the linearly polarized photonic mode in the optical fiber (LP $_0$ 1). The coupling coefficients constitute the physics layer in our model. In the second step, the NN maps the coupling coefficients to the TM $_0$ weight spectra. As shown in Figure 2c, the proposed physics-guided NN with four layers (including

the physics layer) exceeds the maximum accuracy level achieved by the direct NNs. The number of layers for the two stages can be adjusted depending on the complexity of the problem. The advantages of the physics layer with 11 coupling coefficients can be attributed to two aspects: First, the coupling coefficients are in a larger quantity than the design parameters, bridging the vast input—output dimension gap. Second, the output TM_0 weight can be regarded as a composite function

$$K_{pq}, C_{pq}, \chi_p = f_n(d_1, ..., d_m)$$
 (1)

$$w_{\text{TM}_0} = g(K_{\text{pq}}, C_{\text{pq}}, \chi_{\text{p}}) \tag{2}$$

Here, $K_{pq} = \omega \int \int (\varepsilon - \varepsilon_n) E_p^* \cdot E_q dxdy$ is the mode-coupling coefficient from mode p to mode q, $C_{pq} = \int \int \hat{e}_z \cdot (E_p^* \times H_q + E_q)$ $\times H_p^* dxdy$) is the butt coupling coefficient from mode p to mode q, and χ_p is the change in the propagation constant of mode p due to the existence of the neighboring waveguide. E and *H* are normalized electric and magnetic fields, respectively. d_m is the design parameter (details are in the Supporting information). Therefore, inserting coupling coefficients as intermediate variables can guide the orientation to modeling the complex expression of the composite function with physics-based knowledge and relieve the burden for the NN of learning the weights, enabling the use of fewer layers to simplify the NN. It is also worth noting that it is necessary to compute coupling coefficients in simulations to get final TM₀ weight spectra, which means no extra efforts are required to obtain these data.

ON-DEMAND INVERSE DESIGN OF PLASMONIC—PHOTONIC COUPLERS

In the previous works, basic cone shapes with straight side lines in the conic profile are used for convenience, and only the cone angle can be optimized due to the limitations of numerical simulations. There is a clear trade-off in choosing the proper cone angle range, as a small cone angle can reduce the variation rate in phase constant at the vicinity of a coupling region and thus increase the total coupling efficiency, but leads to a long propagation distance toward the tip and consequently a large plasmonic loss. Selectively decreasing the phase constant changing rate at coupling regions can increase the coupling efficiency and lead to new applications such as a bandpass filter. Such designs require more flexibility in designing the waveguide profiles.

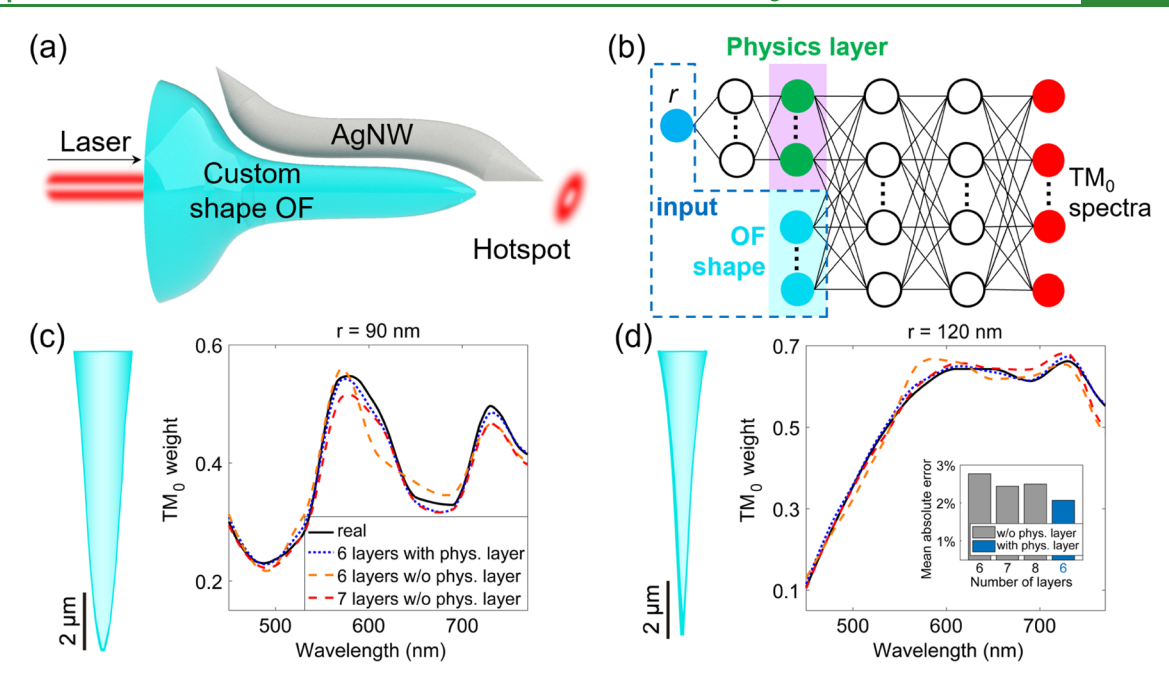


Figure 3. Design of customized-shape couplers. (a) Schematic of an OF-AgNW coupler with arbitrary coupler profiles. (b) Modified NN to include OF profiles as the input. (c) and (d) Forward prediction results with different design parameters. The left panels show the corresponding OF shapes. The inset in (d) shows the MAE of different layer numbers with the physics-guided method (blue) and the traditional method (gray).

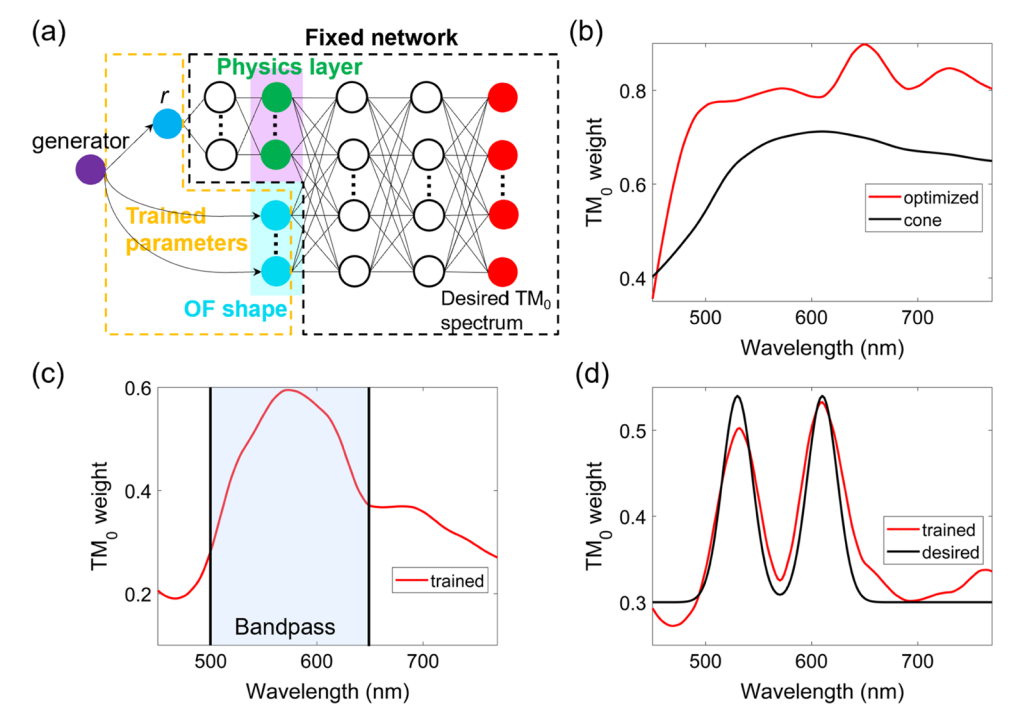


Figure 4. Schematics of the inverse design. (a) Structure of the inverse design NN. (b) TM₀-weight spectra from an optimized arbitrary-shaped coupler (red line) and an optimized cone-shaped coupler (black line). (c) Inverse design for a bandpass filter between 500 and 650 nm. (d) Inverse design for a dual-bandpass filter. Black and red lines represent the desired target and the result obtained by inverse design.

To expand the capability of the NN for the prediction of axisymmetric waveguides with arbitrary profiles, we include OF profiles as a design parameter in training. By varying the edges based on 3rd-order Bezier curves, we generate 300 smooth and monotonic OF profiles, which are included as part of the input in the second layer of the physics-guided network to model the design parameters to the TM_0 intensity spectra, as shown in Figure 3b. We confirm that the performance of the physics-guided network is much better than the traditional network,

including equal or even more layers without the physics layer, as shown in the inner panel of Figure 3d. To predict the optimized OF profile, we perform the inverse design using backpropagation. ⁴⁴ In this method, a new layer with a constant number as the input and design parameters as the weights to be optimized is attached to the trained and fixed forward prediction NN. Since the AgNW radius and the OF profile parameters lie in different layers, they are divided into two separate paths, and the OF profiles are concatenated with

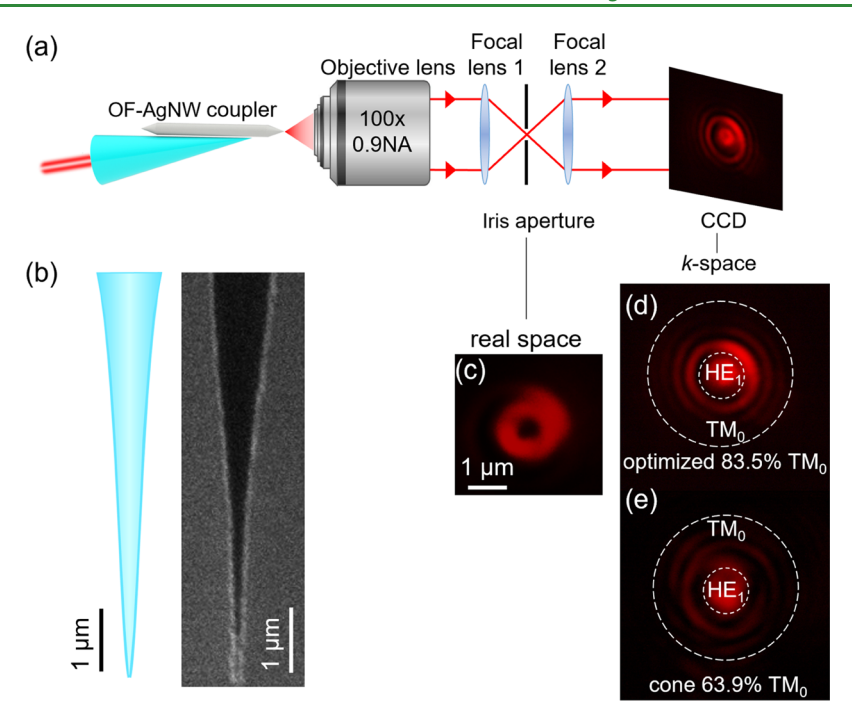


Figure 5. Experimental demonstration of the predicted arbitrary-shaped coupler. (a) Sketch of the *k*-space measurement. (b) Predicted OF profile and the prepared OF. (c) Real-space image of the superfocused spot at the AgNW tip, attached to the designed coupler. (d) and (e) *k*-space images of the predicted arbitrary-shaped probe and an optimized cone-shaped probe. Incident laser: 633 nm in wavelength.

coupling coefficients and merged into the second stage of the NN, as shown in Figure 4a. With a target TM₀ spectrum as the output, OF profile parameters are tuned through the backpropagation. In this process, the figure of merit (FoM) is the mean absolute error (MAE) of the total TM₀ SPP mode weight: $\frac{1}{N}\sum_{\lambda} |w_{\text{predict}}(\lambda) - w_{\text{target}}(\lambda)|$, as the extra penalization for high errors is not desired. And its gradient is analytically obtained by gradient descent algorithms in backpropagation. After certain iterations, the error reaches the minimum, indicating that the available design parameters are the solution to the target response, and the inverse design is accomplished. Although additional training is required for each target spectrum, the whole optimization progress is very fast because the new training set contains only one set of design parameters. Moreover, the backpropagation requires minimal adjustment to the forward NN compared to the tandem network, and no extra algorithm such as the genetic algorithm is needed. By setting unity over all wavelengths as the target for training, we find that an improved coupling efficiency of close to 90% can be achieved. This backpropagation method can also be used to design special couplers that incorporate the single-bandpass or dual-bandpass features by maximizing the target intensity of the TM₀ mode within a specific wavelength range and minimizing them at rest. The results of the inverse design of maximized TM₀, bandpass TM₀ spectra from 500 to 650 nm, and two Gaussian peaks at around 530-610 nm are shown in Figure 4. Interestingly, we notice that in the optimized shape for maximum TM₀ weight, the OF radius shrinks rapidly to the LP₀₁-TM₀ coupling radius, slows down to obtain a long coupling distance, and then shrinks to the tip apex quickly to make the coupling region of LP₀₁-HE₁ short, which maximized the weight of TM₀ mode at the exit.

EXPERIMENTAL DEMONSTRATION

The predicted coupler profile can be prepared by varying the etching time of each section by programming the pulling rate of an OF from the hydrofluoric acid solution (HF, 48%). Figure 5b compares the predicted optimized OF profile and its corresponding outcome fabricated through controlled etching. A 200 nm-in-diameter AgNW is attached to the OF sidewall by a micromanipulator, leaving one end (\sim 5 μ m) protruding outside the OF tip. As shown in Figure 5a, the Fourier-transformed space (k-space) measurement is conducted to confirm the intensity of TM₀ mode in the AgNW waveguide. The radiation pattern of the AgNW forms rings in both the real space (Figure 5c) and the k-space (Figure 5d), indicating that the dominating component is the TM₀ mode. The k-space image is examined by a linear polarizer to identify the boundary between the TM₀ and HE₁ modes (details in the Supporting information), which is labeled by the white-dashed circles in Figure 5d,e. The weight of TM₀ mode in the far-field radiation is defined as the ratio of the TM_0 intensity to the total intensity that contains TM₀, HE₁, and junction scatterings. The same AgNW is used on different OF couplers throughout the measurement to avoid the variation in the far-field radiation efficiency of the TM₀ mode, stemming from the momentum mismatch between the superfocused mode and the free-space scattered light and is thus sensitive to the tip radius. We find that the TM₀ mode weight in k-space increases from 45% on the best conical coupler to 70% on the optimized coupler. Since the protruding length of AgNW outside of the OF is \sim 18 μ m in this measurement (which can be reduced to \sim 2 μ m in real applications), the propagation loss of the TM₀ mode SPP is not ignorable and can be compensated by including the coupling loss (propagation length L_0 $\approx 19 \ \mu \text{m}$ for the TM₀ mode and $L_1 \approx 103 \ \mu \text{m}$ for the HE₁ mode⁴⁶). The TM₀ mode weight near the tip can be acquired through equation:

$$w_{\mathrm{TM}_0} = \frac{w_{\mathrm{TM}_0}(x) \mathrm{e}^{x/L_0}}{w_{\mathrm{TM}_0}(x) \mathrm{e}^{x/L_0} + w_{\mathrm{HE}_{\mathrm{I}}}(x) \mathrm{e}^{x/L_0}}.$$
 After considering the collection

efficiency of the optical microscope and the propagation loss in the protruding region, we estimate that the coupling efficiency for ${\rm TM_0}$ mode is improved from 63.9% from the conical coupler to 83.5% from the optimized coupler.

CONCLUSIONS

In summary, we propose a two-stage physics-guided NN to bridge the input-output mismatch and accelerate the network structure for plasmonic application designs. The proposed physics-guided network combines the advantages of the highefficiency data-driven machine learning method and the informative physics-based analytical model. Moreover, we utilize backpropagation and gradient descent algorithms to optimize the design parameters by training the modified forward prediction network with a certain target as the output, providing a simple and fast approach for inverse designs. The high-efficiency high-accuracy physics-guided NN allows us to model the complex electromagnetic responses with a simple architecture and can be applied to other research fields of materials science, in which physics models serve as intermediate parameters.

METHODS

COMSOL Multiphysics is employed to complete the numerical simulations to obtain the electromagnetic field distributions, and the TM₀ SPP mode intensity spectra are calculated by solving the partial differential equations of the coupled-mode theory. The complex permittivity values of silver are obtained from Johnson and Christy.⁴ The spectra cover the visible-light region from 450 to 770 nm at 161 isometric wavelengths. In the cone-shaped fiber situation, the AgNW radius sampling ranges from 75 to 145 nm with a step of 5 nm and the fiber tip angle sampling ranges from 4 to 20° with a step of 1°. This combination generates 255 samples, 204 of which are randomly selected for training, and the remaining 51 of them are used for testing. In the customized-shape optimization, the selections of AgNW radius remain the same. Three hundred pieces of smooth and monotonic OF profiles are constructed using 3rd-order Bezier curves with two control points. The expression of the Bezier curve is B(t) = $(1-t)^3P_0 + 3(1-t)^2tP_1 + 3(1-t)t^2P_2 + t^3P_3$. Here, P_0 and P_3 are the two ends of the curve, P_1 , P_2 are the control points, and t is a variable between 0 and 1. Four thousand and five hundred samples are collected in the simulations, 3600 of them are randomly selected for training, and the remaining 900 of them are used for testing. The NN models are constructed by the deep learning module of MATLAB MathWorks.

For the experimental demonstrations, the AgNWs are synthesized by the polyol reduction method 48-50 and attached to the OF by a tungsten tip. In the k-space measurement, a 633 nm laser was coupled to the AgNW from the OF. An optical microscope (Nikon Eclipse Ni-U) with a 100× microscope objective having a numerical aperture of 0.9 was used to collect the light at the AgNW tip apex. A lens with a focal length of 10 cm is added behind the microscope to operate Fourier transform to k-space. And a colored CCD camera (AmScope MU1803) was used to collect and capture the k-space images.

ASSOCIATED CONTENT

Supporting Information

The Supporting Information is available free of charge at https://pubs.acs.org/doi/10.1021/acsami.2c05083.

> Improved coupled-mode theory used in the simulations; construction and training of the prediction network; backpropagation method for the optimization; full-wave simulations to verify the optimized coupler shapes; kspace measurement (PDF)

AUTHOR INFORMATION

Corresponding Author

Ming Liu - Materials Science and Engineering program, University of California—Riverside, Riverside, California 92521, United States; Department of Electrical and

Computer Engineering, University of California—Riverside, Riverside, California 92521, United States; oorcid.org/ 0000-0001-9849-1845; Email: ming@ece.ucr.edu

Authors

- Boqun Liang Materials Science and Engineering program, University of California-Riverside, Riverside, California 92521, United States; o orcid.org/0000-0002-1163-2244
- Da Xu Department of Electrical and Computer Engineering, University of California—Riverside, Riverside, California 92521, United States; orcid.org/0000-0002-7554-426X
- Ning Yu Department of Chemical and Environmental Engineering, University of California—Riverside, Riverside, California 92521, United States
- Yaodong Xu Materials Science and Engineering program, University of California—Riverside, Riverside, California 92521, United States
- **Xuezhi Ma** Department of Electrical and Computer Engineering, University of California—Riverside, Riverside, California 92521, United States; o orcid.org/0000-0003-3607-1145
- **Qiushi Liu** Department of Electrical and Computer Engineering, University of California-Riverside, Riverside, California 92521, United States; o orcid.org/0000-0002-9017-2492
- M. Salman Asif Department of Electrical and Computer Engineering and Department of Computer Science and Engineering, University of California—Riverside, Riverside, California 92521, United States
- Ruoxue Yan Materials Science and Engineering program, University of California-Riverside, Riverside, California 92521, United States; Department of Chemical and Environmental Engineering, University of California— Riverside, Riverside, California 92521, United States; orcid.org/0000-0002-0034-9806

Complete contact information is available at: https://pubs.acs.org/10.1021/acsami.2c05083

The authors declare no competing financial interest.

ACKNOWLEDGMENTS

M.L. acknowledges support from the National Science Foundation (nos. 1654746 and 1810453). R.Y. acknowledges support by NSF award no. 1654794. M.S.A. acknowledges support from the Air Force Office of Scientific Research (AFOSR) (FA9550-21-1-0330).

REFERENCES

- (1) Jiang, R.-H.; Chen, C.; Lin, D.-Z.; Chou, H.-C.; Chu, J.-Y.; Yen, T.-J. Near-Field Plasmonic Probe with Super Resolution and High Throughput and Signal-to-Noise Ratio. Nano Lett. 2018, 18, 881-
- (2) Lerman, G. M.; Yanai, A.; Levy, U. Demonstration of Nanofocusing by the use of Plasmonic Lens Illuminated with Radially Polarized Light. Nano Lett. 2009, 9, 2139-2143.
- (3) Gupta, P.; Luan, J.; Wang, Z.; Cao, S.; Bae, S. H.; Naik, R. R.; Singamaneni, S. On-Demand Electromagnetic Hotspot Generation in Surface-Enhanced Raman Scattering Substrates via "Add-On" Plasmonic Patch. ACS Appl. Mater. Interfaces 2019, 11, 37939-37946. (4) Yadav, R. K.; Bourgeois, M. R.; Cherqui, C.; Juarez, X. G.; Wang, W.; Odom, T. W.; Schatz, G. C.; Basu, J. K. Room Temperature Weak-to-Strong Coupling and the Emergence of Collective Emission

- from Quantum Dots Coupled to Plasmonic Arrays. ACS Nano 2020, 14, 7347–7357.
- (5) Lu, C.; Hu, X.; Yang, H.; Gong, Q. Chip-integrated ultrawide-band all-optical logic comparator in plasmonic circuits. *Sci. Rep.* **2015**, 4. No. 3869
- (6) Koch, U.; Uhl, C.; Hettrich, H.; Fedoryshyn, Y.; Hoessbacher, C.; Heni, W.; Baeuerle, B.; Bitachon, B. I.; Josten, A.; Ayata, M.; Xu, H.; Elder, D. L.; Dalton, L. R.; Mentovich, E.; Bakopoulos, P.; Lischke, S.; Krüger, A.; Zimmermann, L.; Tsiokos, D.; Pleros, N.; Möller, M.; Leuthold, J. A monolithic bipolar CMOS electronic—plasmonic high-speed transmitter. *Nat. Electron.* **2020**, *3*, 338–345.
- (7) Fernandez-Bravo, A.; Wang, D.; Barnard, E. S.; Teitelboim, A.; Tajon, C.; Guan, J.; Schatz, G. C.; Cohen, B. E.; Chan, E. M.; Schuck, P. J.; Odom, T. W. Ultralow-threshold, continuous-wave upconverting lasing from subwavelength plasmons. *Nat. Mater.* **2019**, *18*, 1172–1176.
- (8) Lee, J.-H.; Lee, J. H.; Xiao, J.; Desai, M. S.; Zhang, X.; Lee, S.-W. Vertical Self-Assembly of Polarized Phage Nanostructure for Energy Harvesting. *Nano Lett.* **2019**, *19*, 2661–2667.
- (9) Liu, Y.; Teitelboim, A.; Fernandez-Bravo, A.; Yao, K.; Altoe, M. V. P.; Aloni, S.; Zhang, C.; Cohen, B. E.; Schuck, P. J.; Chan, E. M. Controlled Assembly of Upconverting Nanoparticles for Low-Threshold Microlasers and Their Imaging in Scattering Media. ACS Nano 2020, 14, 1508–1519.
- (10) Berweger, S.; Atkin, J. M.; Olmon, R. L.; Raschke, M. B. Adiabatic Tip-Plasmon Focusing for Nano-Raman Spectroscopy. *J. Phys. Chem. Lett.* **2010**, *1*, 3427–3432.
- (11) Gramotnev, D. K.; Vogel, M. W.; Stockman, M. I. Optimized nonadiabatic nanofocusing of plasmons by tapered metal rods. *J. Appl. Phy.* **2008**, *104*, No. 034311.
- (12) Zhang, T.; Callard, S.; Jamois, C.; Chevalier, C.; Feng, D.; Belarouci, A. Plasmonic-photonic crystal coupled nanolaser. *Nanotechnology* **2014**, *25*, No. 315201.
- (13) Hu, D. J. J.; Ho, H. P. Recent advances in plasmonic photonic crystal fibers: design, fabrication and applications. *Adv. Opt. Photon.* **2017**, *9*, 257–314.
- (14) Hassan, S.; Chack, D.; Mahajan, V. High extinction ratio and low loss polarization beam splitter based on multimode interference for PICs. *Appl. Opt.* **2020**, *59*, 3369–3375.
- (15) Kim, S.; Yu, N.; Ma, X.; Zhu, Y.; Liu, Q.; Liu, M.; Yan, R. High external-efficiency nanofocusing for lens-free near-field optical nanoscopy. *Nat. Photonics* **2019**, *13*, 636–643.
- (16) Novotny, L. Strong coupling, energy splitting, and level crossings: A classical perspective. Am. J. Phys. 2010, 78, 1199–1202.
- (17) Malkiel, I.; Mrejen, M.; Nagler, A.; Arieli, U.; Wolf, L.; Suchowski, H. Plasmonic nanostructure design and characterization via Deep Learning. *Light: Sci. Appl.* **2018**, *7*, No. 60.
- (18) Ma, W.; Xu, Y.; Xiong, B.; Deng, L.; Peng, R.-W.; Wang, M.; Liu, Y. Pushing the Limits of Functionality-Multiplexing Capability in Metasurface Design Based on Statistical Machine Learning. *Adv. Mater.* **2022**, 34, No. 2110022.
- (19) Ma, W.; Cheng, F.; Xu, Y.; Wen, Q.; Liu, Y. Probabilistic Representation and Inverse Design of Metamaterials Based on a Deep Generative Model with Semi-Supervised Learning Strategy. *Adv. Mater.* **2019**, *31*, No. 1901111.
- (20) Ma, W.; Liu, Z.; Kudyshev, Z. A.; Boltasseva, A.; Cai, W.; Liu, Y. Deep learning for the design of photonic structures. *Nat. Photonics* **2021**, *15*, 77–90.
- (21) Xu, Y.; Zhang, X.; Fu, Y.; Liu, Y. Interfacing photonics with artificial intelligence: an innovative design strategy for photonic structures and devices based on artificial neural networks. *Photon. Res.* **2021**, *9*, B135–B152.
- (22) Wiecha, P. R.; Arbouet, A.; Girard, C.; Muskens, O. L. Deep learning in nano-photonics: inverse design and beyond. *Photon. Res.* **2021**. 9. B182–B200.
- (23) Jiang, J.; Chen, M.; Fan, J. A. Deep neural networks for the evaluation and design of photonic devices. *Nat. Rev. Mater.* **2021**, *6*, 679–700.

- (24) Jiang, J.; Sell, D.; Hoyer, S.; Hickey, J.; Yang, J.; Fan, J. A. Free-Form Diffractive Metagrating Design Based on Generative Adversarial Networks. *ACS Nano* **2019**, *13*, 8872–8878.
- (25) Goh, G. B.; Hodas, N. O.; Vishnu, A. Deep learning for computational chemistry. *J. Comput. Chem.* **2017**, *38*, 1291–1307.
- (26) Wu, Y.-J.; Fang, L.; Xu, Y. Predicting interfacial thermal resistance by machine learning. *npj Comput. Mater.* **2019**, 5, No. 56.
- (27) Qu, Y.; Jing, L.; Shen, Y.; Qiu, M.; Soljačić, M. Migrating Knowledge between Physical Scenarios Based on Artificial Neural Networks. *ACS Photonics* **2019**, *6*, 1168–1174.
- (28) Opgenorth, P.; Costello, Z.; Okada, T.; Goyal, G.; Chen, Y.; Gin, J.; Benites, V.; de Raad, M.; Northen, T. R.; Deng, K.; Deutsch, S.; Baidoo, E. E. K.; Petzold, C. J.; Hillson, N. J.; Garcia Martin, H.; Beller, H. R. Lessons from Two Design—Build—Test—Learn Cycles of Dodecanol Production in Escherichia coli Aided by Machine Learning. ACS Synth. Biol. 2019, 8, 1337—1351.
- (29) Ma, W.; Cheng, F.; Liu, Y. Deep-Learning-Enabled On-Demand Design of Chiral Metamaterials. *ACS Nano* **2018**, *12*, 6326–6334.
- (30) Liu, D.; Tan, Y.; Khoram, E.; Yu, Z. Training Deep Neural Networks for the Inverse Design of Nanophotonic Structures. *ACS Photonics* **2018**, *5*, 1365–1369.
- (31) Tanriover, I.; Hadibrata, W.; Aydin, K. Physics-Based Approach for a Neural Networks Enabled Design of All-Dielectric Metasurfaces. *ACS Photonics* **2020**, *7*, 1957–1964.
- (32) Wen, F.; Jiang, J.; Fan, J. A. Robust Freeform Metasurface Design Based on Progressively Growing Generative Networks. *ACS Photonics* **2020**, *7*, 2098–2104.
- (33) Jiang, J.; Fan, J. A. Global Optimization of Dielectric Metasurfaces Using a Physics-Driven Neural Network. *Nano Lett.* **2019**, *19*, 5366–5372.
- (34) Liu, Z.; Zhu, D.; Rodrigues, S. P.; Lee, K.-T.; Cai, W. Generative Model for the Inverse Design of Metasurfaces. *Nano Lett.* **2018**. *18*. 6570–6576.
- (35) Yeung, C.; Tsai, J.-M.; King, B.; Kawagoe, Y.; Ho, D.; Knight, M. W.; Raman, A. P. Elucidating the Behavior of Nanophotonic Structures through Explainable Machine Learning Algorithms. *ACS Photonics* **2020**, *7*, 2309–2318.
- (36) Unni, R.; Yao, K.; Zheng, Y. Deep Convolutional Mixture Density Network for Inverse Design of Layered Photonic Structures. *ACS Photonics* **2020**, *7*, 2703–2712.
- (37) Huntington, M. D.; Lauhon, L. J.; Odom, T. W. Subwavelength Lattice Optics by Evolutionary Design. *Nano Lett.* **2014**, *14*, 7195–7200
- (38) An, S.; Fowler, C.; Zheng, B.; Shalaginov, M. Y.; Tang, H.; Li, H.; Zhou, L.; Ding, J.; Agarwal, A. M.; Rivero-Baleine, C.; Richardson, K. A.; Gu, T.; Hu, J.; Zhang, H. A Deep Learning Approach for Objective-Driven All-Dielectric Metasurface Design. *ACS Photonics* **2019**, *6*, 3196–3207.
- (39) Kim, Y.; Yang, C.; Kim, Y.; Gu, G. X.; Ryu, S. Designing an Adhesive Pillar Shape with Deep Learning-Based Optimization. *ACS Appl. Mater. Interfaces* **2020**, *12*, 24458–24465.
- (40) Jin, W.; Li, W.; Orenstein, M.; Fan, S. Inverse Design of Lightweight Broadband Reflector for Relativistic Lightsail Propulsion. *ACS Photonics* **2020**, *7*, 2350–2355.
- (41) Minkov, M.; Williamson, I. A. D.; Andreani, L. C.; Gerace, D.; Lou, B.; Song, A. Y.; Hughes, T. W.; Fan, S. Inverse Design of Photonic Crystals through Automatic Differentiation. *ACS Photonics* **2020**, *7*, 1729–1741.
- (42) Kao, C. Y.; Osher, S.; Yablonovitch, E. Maximizing band gaps in two-dimensional photonic crystals by using level set methods. *Appl. Phys. B* **2005**, *81*, 235–244.
- (43) Andkjær, J.; Nishiwaki, S.; Nomura, T.; Sigmund, O. Topology optimization of grating couplers for the efficient excitation of surface plasmons. *J. Opt. Soc. Am. B* **2010**, *27*, 1828–1832.
- (44) Peurifoy, J.; Shen, Y.; Jing, L.; Yang, Y.; Cano-Renteria, F.; DeLacy, B. G.; Joannopoulos, J. D.; Tegmark, M.; Soljačić, M. Nanophotonic particle simulation and inverse design using artificial neural networks. *Sci. Adv.* **2018**, *4*, No. eaar4206.

- (45) Vai, M. M.; Shuichi, W.; Bin, L.; Prasad, S. Reverse modeling of microwave circuits with bidirectional neural network models. IEEE Trans. Microwave Theory Tech. 1998, 46, 1492-1494.
- (46) Kim, S.; Bailey, S.; Liu, M.; Yan, R. Decoupling co-existing surface plasmon polariton (SPP) modes in a nanowire plasmonic waveguide for quantitative mode analysis. Nano Res. 2017, 10, 2395-2404.
- (47) Johnson, P. B.; Christy, R. W. Optical Constants of the Noble Metals. Phys. Rev. B 1972, 6, 4370-4379.
- (48) Liu, Q.; Kim, S.; Ma, X.; Yu, N.; Zhu, Y.; Deng, S.; Yan, R.; Zhao, H.; Liu, M. Ultra-sharp and surfactant-free silver nanowire for scanning tunneling microscopy and tip-enhanced Raman spectroscopy. Nanoscale 2019, 11, 7790-7797.
- (49) Ma, X.; Zhu, Y.; Kim, S.; Liu, Q.; Byrley, P.; Wei, Y.; Zhang, J.; Jiang, K.; Fan, S.; Yan, R.; Liu, M. Sharp-Tip Silver Nanowires Mounted on Cantilevers for High-Aspect-Ratio High-Resolution Imaging. Nano Lett. 2016, 16, 6896-6902.
- (50) Ma, X.; Zhu, Y.; Yu, N.; Kim, S.; Liu, Q.; Apontti, L.; Xu, D.; Yan, R.; Liu, M. Toward High-Contrast Atomic Force Microscopy-Tip-Enhanced Raman Spectroscopy Imaging: Nanoantenna-Mediated Remote-Excitation on Sharp-Tip Silver Nanowire Probes. Nano Lett. **2019**, *19*, 100–107.

☐ Recommended by ACS

Struca tnuCdrpeti Poraolp & reglioc 22 DP olna smonic Phot 6 n iy s Ft aa bb rs i bc y 6 th ea dd Sopwhere Lithography

Yanfeng Wang,etYiapli.ng Zhao, DECEMBER 06, 2022 ACS APPLIED NANO MATERIALS

ConcurOrpet nitmi a fait f fan Taic et find on Birin ar y Pha Nordaes fko Trhr-Beiemens Naonnoaplatter ning

Chihun Lee, et Juan/suk Rho, OCTOBER 13, 2022 ACS PHOTONICS

R F AM

Ther Chahtor Poll as mSounrifotaactetRieosoon ances

Jussi Kelavuori*ęt Mail*k.ko J. Huttunen, MAY 04, 2022 NANO LETTERS R E A□

Four-Einegrin & eta es othLoantit Riecs eon ances

Theng-Loo Lim, eRobert W. MARCH 31, 2022 ACS NANO

Get More Suggestions

Supporting Information for:

Physics-guided neural-network-based inverse design of a photonic-plasmonic nanodevice for superfocusing

Boqun Liang¹, Da Xu², Ning Yu³, Yaodong Xu¹, Xuezhi Ma², Qiushi Liu², M. Salman Asif^{2,4}, Ruoxue Yan^{1,3}, Ming Liu^{1,2,*}

Addresses:

- ¹ Materials Science and Engineering program, University of California Riverside, Riverside, California 92521, United States
- ² Department of Electrical and Computer Engineering, University of California Riverside, Riverside, California 92521, United States
- ³ Department of Chemical and Environmental Engineering, University of California Riverside, Riverside, California 92521, United States
- ⁴ Department of Computer Science and Engineering, University of California Riverside, Riverside, California 92521, United States

KEYWORDS:

deep learning, neural network, superfocusing, plasmonic, on-demand design, silver nanowire

Email: mingliu@ucr.edu

1. Improved coupled-mode theory used in the simulations:

In the AgNW-OF hybrid system, the SPP modes in the AgNW waveguide are strongly coupled with the fiber mode in the tapered OF since the two waveguides are closely packed. Therefore, the widely used coupled-mode theory that considers only the weak coupling between two separated waveguides is insufficient. We developed codes based on the improved coupled-mode theory that considers not only the mode coupling coefficients between two waveguides, but also the butt coupling coefficients and the change in propagation constant. Now the general evolution of the three modes (two SPP modes: TM₀, HE₁, and one OF mode: LP₀₁ is determined by the following generalized coupled-mode equations¹:

$$\frac{\mathrm{d}}{\mathrm{d}} \begin{pmatrix} () \\ () \\ () \end{pmatrix} = \begin{pmatrix} + \frac{+}{2} \\ + \frac{0}{2} \\ 0 + \frac{0}{2} \end{pmatrix} \begin{pmatrix} () \\ () \\ () \end{pmatrix} \#(\mathrm{S1})$$

(, and (are the normalized amplitudes of the electromagnetic field of mode LP_{01} , TM_0 and HE_1 , respectively. is the coordinate on the propagation direction. (= , ,) is the propagation constant. $=\frac{1}{1+|l|^2}$, $=\frac{1}{1+|l|^2}$, and $=\frac{1}{1+|l|^2}$, $\frac{1}{1+|p|^2}$. Here, = () · d d is the mode coupling coefficient from mode p to mode q, = \cdot (\times + \times)d d is the butt coupling coefficient from mode p to mode q_1 = () · d d is the change in propagation constant due to the are normalized electric and magnetic fields. existence of the neighbor waveguide. and respectively, which are obtained from the mode analysis performed by the finite element method (COMSOL Multiphysics). p and q refer to mode a, b and c. is the permittivity containing both is the permittivity with only the OF, = is the permittivity with only the waveguides, AgNW. It is worth noting that in our configurations the two waveguides strongly perturbate the mode profile of each other, resulting in nonzero and that modifies both and Therefore, the improved coupled-mode theory instead of the conventional simplified coupledmode theory is required, which includes the influence from nontrivial and The differential equations in eq. S1 are calculated using an ordinary differential equation (ODE) solver (Matlab MathWorks, ode45).

2. Construction and training of the prediction network

Conical OF case. For training both the direct and physics-guided deep learning models, the Adam optimization algorithm² for stochastic gradient descent is applied. An initial learn rate of 0.001, weight learn rate factor of 0.1, a batch size of 51, and a maximum epoch of 10000 is adopted. Each fully connected layer has 100 units and is followed by an activation function. The activation functions of tanh, RELU, and LRELU are tested respectively. In the regression task, root mean square error (RMSE) loss function is used.

In the first stage of the prediction network, the input is the AgNW radius r and the OF taper angle (the dimension is 2), and the output is the mode and butt coupling coefficients and the change in phase constant (, , , , the dimension is 11). In the second stage, the input is the , , , the output is the TM_0 mode weight spectra with a step of 2 nm from 450 nm to 770 nm (the dimension is 161).

Custom shape OF case. For training both the direct and physics-guided deep learning models, the Adam optimization algorithm is applied. An initial learn rate of 0.001, weight learn rate factor of 0.1, a batch size of 600, and a maximum epoch of 20000 is adopted. Each fully connected layer has 100 units and is followed by a tanh activation function. In the regression task, root mean square error (RMSE) loss function is used.

In the first stage of the prediction network, the input is the AgNW radius r (the dimension is 1), and the output is the $\,$, $\,$, (the dimension is 11). The optical fiber shape is represented by a Bezier curve controlled by 5 points. In the second stage of the prediction network, the coefficients in CMT are concatenated with the vertical ordinates and the interval of horizontal ordinates of the control points of the OF shape and form the input (the dimension is 17). And the output is the TM_0 mode weight spectra (the dimension is 161).

3. Backpropagation method for the optimization

A generator with a constant 1 as the first layer and the parameters to be optimized as training weights is attached to the trained and fixed prediction network. The target is the desired TM_0 mode weight spectrum. An initial learn rate of 0.05, weight learn rate factor of 1, the batch size is the quantity of desired spectra, and a maximum epoch of 10000 is adopted. During the learning process, the error is propagated backward, and the design parameters are adjusted by gradient descent. When the training ends, the error between the target is minimized, which means the design parameters are optimized.

4. Full-wave simulations to verify the optimized coupler shapes

To further confirm the improvement of the coupling efficiency, we conducted numerical simulations (COMSOL Multiphysics) to compare an optimized cone-shaped coupler with the predicted arbitrary-shaped coupler, as shown in Fig. S1. The linearly polarized light is launched from the tapered fiber. The cone-shaped coupler has an optimized tip angle (10 $^{\circ}$) and an optimized AgNW radius (100 nm). This configuration has a TM₀ SPP mode weight of 63%. In comparison, the optimized arbitrary-shaped coupler can reach as high as 89% in the TM₀ SPP mode.

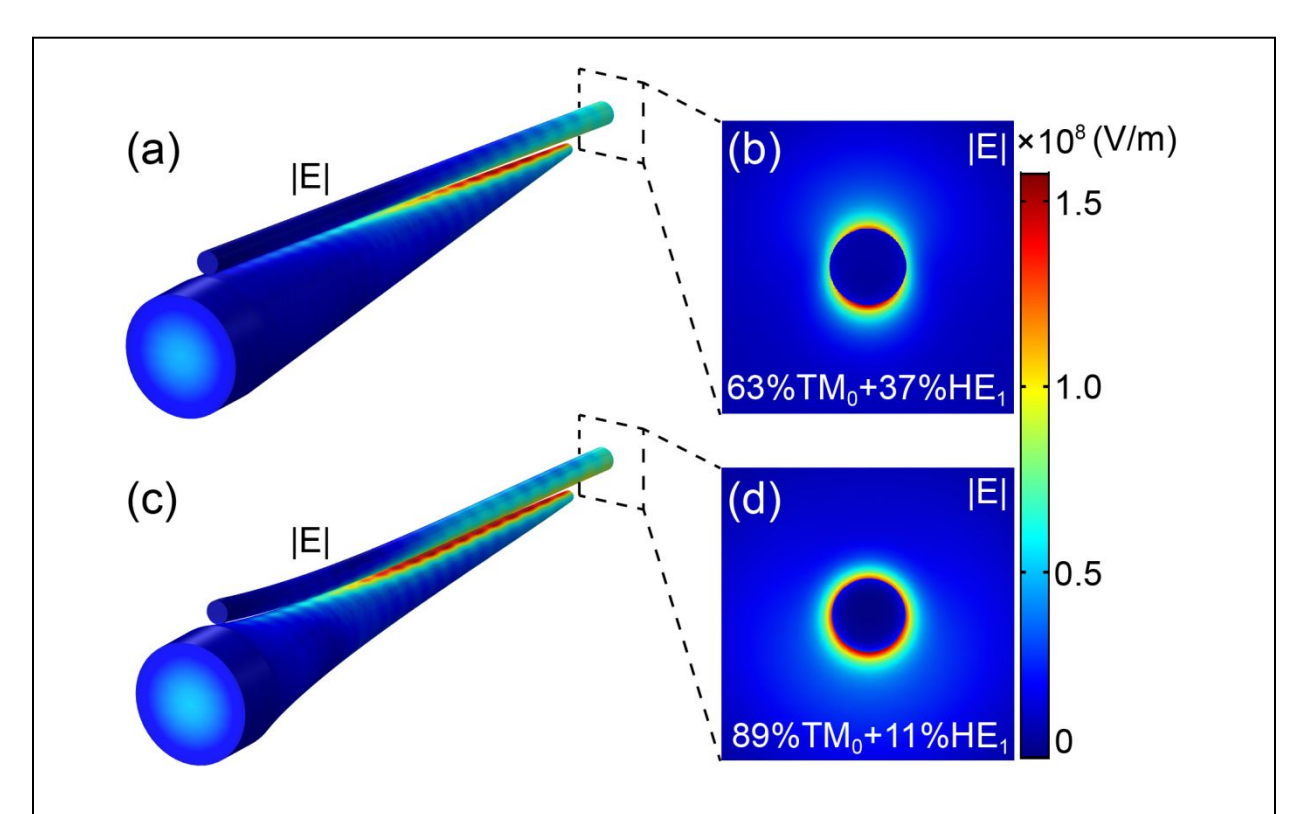


Fig. S1 Confirmation of TM₀ SPP mode weights of cone and optimized-shape optical fiber calculated by COMSOL. (a, b) Electric field distribution on the surfaces of the cone optical fiber and silver nanowire (a) and the cross-section near the end of the silver nanowire (b). (c, d) Electric field distribution on the surfaces of the optimized-shape optical fiber and silver nanowire (c) and the cross-section near the end of the silver nanowire (d).

5. k-space measurement

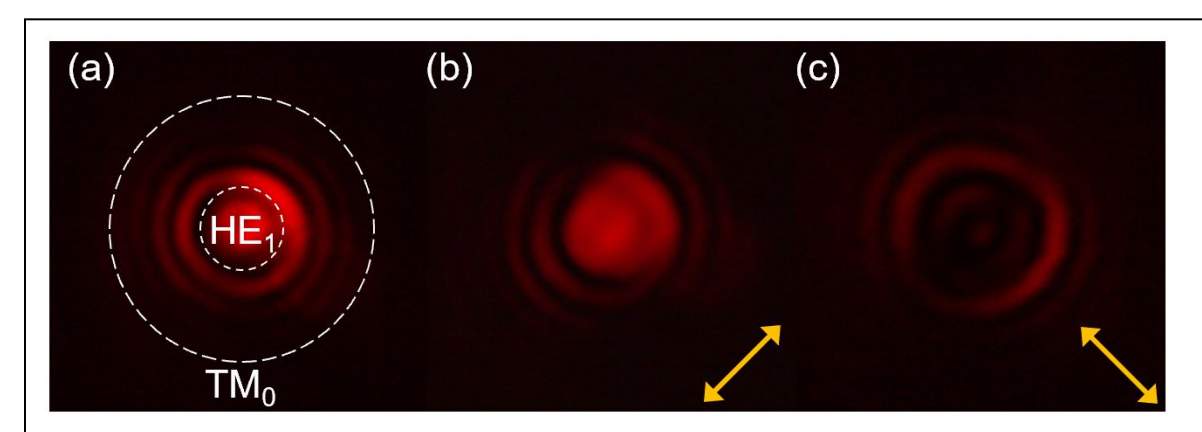


Fig. S2 Polarization resolved *k***-space images.** (a) The *k*-space image without the polarizer. (b-c) *k*-space images with a linear polarizer, with the extinction direction as the yellow arrows show.

We measured the proportion of TM_0 mode intensity in k-space where TM_0 and HE_1 are spatially separated. The central circle corresponds to the linearly polarized HE_1 mode, and the outer ring corresponds to the radially polarized TM_0 mode. The polarization direction of HE_1 mode is the same as the yellow arrow in Fig. S2b. The intensity of the central circle minimizes when the polarizer is altered to the perpendicular direction as shown in Fig. S2c.

References

- 1. Chuang, S. L., *Physics of Optoelectronic Devices*. Wiley: 1995.
- 2. Kingma, D. P.; Ba, J., Adam: A Method for Stochastic Optimization. In *3rd International Conference on Learning Representations*, San Diego, 2015.